

# **Electron-Phonon Coupling Mediated by Fröhlich Interaction in $\text{Rb}_2\text{SnBr}_6$ Perovskite**

C. C. S. Soares <sup>1</sup>, J. S. Rodríguez-Hernández <sup>1</sup>, Bruno P. Silva <sup>2</sup>, Mayra A. P. Gómez  
<sup>1</sup>, V. S. Neto <sup>1</sup>, A. P. Ayala <sup>1</sup>, and C.W.A. Paschoal <sup>1,\*</sup>.

<sup>1</sup> Departamento de Física, Universidade Federal do Ceará, Campus do Pici, 65455-900, Fortaleza - CE, Brazil.

<sup>2</sup> Instituto Federal de Educação, Ciência e Tecnologia do Ceará, Campus Camocim, 62400-000, Camocim - CE, Brazil.

\*Corresponding author. E-mail address: [paschoal.william@fisica.ufc.br](mailto:paschoal.william@fisica.ufc.br)

## ABSTRACT

Due to their well-suited optoelectronic properties, metal halide perovskites are emerging semiconductor materials with potential applications in solar cells, detectors, and light-emitting diodes. Beyond the traditional 3D perovskites, low-dimensional counterparts have more attractive effects, such as excitonic emissions and quantum confinement that are enhanced by the reduced dimensionality, which involve the Electron-Phonon Coupling (EPC). Such phenomenon, which comprehends the interaction between charge carriers and lattice vibrations, usually strongly impacts the photoluminescence (PL) response in low-dimensional frameworks. In this paper, we investigated the intrinsic EPC onto low-temperature PL of the zero-dimensional (0D)  $\text{Rb}_2\text{SnBr}_6$  perovskite. Temperature-dependent PL measurements, complemented by various characterization techniques and theoretical calculations, revealed broadband emission with a significant Stokes shift attributed to self-trapped excitons (STEs). The Fröhlich mechanism, mediated by interactions between excitonic charge carriers and longitudinal optical (LO) phonons, primarily accounts for the emission broadening through phonon-assisted radiative recombination. The EPC strength was evaluated through the Huang-Rhys factor  $S = 34$ , confirming strong correlations between electronic and vibrational properties and supporting the STE emission assumption. The possible mechanism of STE formation was evaluated by the Fröhlich parameter  $\alpha$  of 1.94 for electrons and 4.73 for holes, which points out a major contribution of the hole-polaron quasi-particle on exciton trapping. Our findings give insights regarding the influence of EPC in 0D perovskites and STE formation, which leads to the assessment of  $\text{Rb}_2\text{SnBr}_6$  for light-harvesting applications.

**Keywords:** Electron-Phonon Coupling; Self-Trapped Excitons; Fröhlich Interactions.

## I. INTRODUCTION

For the past few years, Metal Halide Perovskites (MHP) have been extensively investigated due to their remarkable optoelectronic properties as tunable bandgap energy, intense light absorption, and efficient charge transport, which are convenient for photovoltaic applications such as solar cells, detectors, and light-emitting diodes (LEDs) devices<sup>1-3</sup>. Beyond traditional three-dimensional (3D) perovskites, low-dimensional variants comprising 2D, 1D, and 0D structures have attracted attention for their distinctive superior stability, excitonic behavior, and quantum confinement effects, which are one of the consequences of the reduced dielectric screening emerged from lowering dimensionality<sup>4-6</sup>, resulting in stronger electron-hole interactions and larger exciton binding energies that can remain stable even at room temperature, leading to modified charge transport and enhanced radiative decay rates<sup>7-9</sup>.

One of the most intriguing factors that influence the optoelectronic behavior of MHP is the Electron-Phonon Coupling (EPC), which underlies the interaction between charge carriers and lattice vibrations and has a compelling role in carrier mobility and phonon-assisted radiative recombination<sup>10-16</sup>. EPC is enhanced in low-dimensional MHP, often triggering carrier localization through a quasi-particle called polaron formed by the carrier and its own polarization field that can be thought of as an electron (or hole) moving slowly by dressing itself with a phonon cloud<sup>17-20</sup>, and becoming localized. Although excitons are neutral quasi-particles, carrier localization can also restrain their movements along the lattice and create self-trapped excitons (STE)<sup>21-23</sup>. The electron-phonon interactions in polaron formation of polar perovskites can be described by theoretical models like the Fröhlich interaction<sup>10,24-26</sup>, which accounts for the coupling between charge carriers and longitudinal optical (LO) phonons where the Fröhlich parameter  $\alpha$ <sup>27</sup>, dictates the interaction strength between carries with LO vibrations. In the case of excitonic emissions, the coupling strength can also be quantified by the Huang-Rhys factor  $S$ <sup>28,29</sup>, which can be extracted from temperature-dependent photoluminescence (PL) spectra by analyzing the phonon contributions to PL linewidth broadening<sup>30,31</sup>. Experimentally, temperature-dependent PL, Raman, and IR spectroscopies have been widely used to investigate EPC<sup>32-34</sup>, providing essential information on phonon modes and their influence on the optical response.

Vacancy-ordered 0D perovskites depicted by the chemical formula  $A_2BX_6$  offer a unique crystal structure feasible for investigating the EPC in low-dimensional MHP<sup>35,36</sup>. They consist of an isolated  $[BX_6]$  octahedra arrangement among a framework composed of the A-cations. The isolated configuration provides a more favorable environment for charge carriers to interact with lattice vibrations since the octahedra are not as constrained together as their high-dimensional counterparts, amplifying the effects concerning the charge carriers-vibrations interplay and quantum confinement<sup>37,38</sup>, which usually results in a broadband emission with large Stokes-shift from STE resulting in high PL quantum yields<sup>39</sup>. Furthermore, the optoelectronic phenomena concerning the 0D perovskites are intimately related to the isolated octahedra units where the surroundings A-cations not only have minimum effects on the electronic band structure of the octahedra (which maintains their photophysical properties) but also increase considerably these perovskites stability upon air exposure protecting the metal halide octahedral anions<sup>35</sup>. All these features have shown the potential applications of 0D perovskites in LED lighting, sensors, and X-ray scintillation<sup>40,41</sup>.

Understanding the mechanisms involved in the EPC of 0D perovskites is essential for their optoelectronic applications, which creates opportunities for a range of possibilities, from the fundamentals to device engineering. Thus, in this paper, we investigated the EPC and its influence on the PL emission of  $Rb_2SnBr_6$  vacancy-ordered 0D perovskite. We discuss the EPC strength, its main mechanism, and its major role on the PL origin and linewidth broadening with the aid of several characterization techniques and theoretical calculations. Our results elucidate strong EPC via Fröhlich interactions with LO phonons undergoing low-temperature STE emission of  $Rb_2SnBr_6$  characteristic of polar inorganic perovskites.

## II. EXPERIMENTAL AND COMPUTATIONAL METHODS

**Synthesis Method:** Light-yellow  $\text{Rb}_2\text{SnBr}_6$  single crystals were grown through the slow evaporation method: 48 mg (0.18 mmol) of  $\text{Rb}_2\text{SO}_4$  (289280: Sigma-Aldrich) and 50 mg (0.18 mmol) of  $\text{SnBr}_2$  (309257: Sigma-Aldrich) were dissolved using hydrobromic acid (47 wt% in  $\text{H}_2\text{O}$ ) (5 mL) and distilled water (5 mL). The solution was heated at 80 °C for 1 hour under rigorous stirring and then cooled slowly to room temperature in a beaker sealed with paraffin film. Clear light-yellow microcrystals grown at the bottom of the beaker were collected and cleaned with ethyl ether and dried overnight at 60 °C in a vacuum furnace.

**Single Crystal X-Ray Diffraction:** Crystal structure determination was conducted using single crystal X-ray diffraction (SCXRD) performed on a Bruker D8 Venture X-ray Kappa diffractometer equipped with a Photon II detector and Mo  $\text{K}\alpha$  radiation ( $\lambda = 0.71073 \text{ \AA}$ ) microfocus source. A crystal sample was mounted on a MiTeGen MicroMount using immersion oil. The APEX 4 software was used for unit cell determination and data collection. The data reduction and global cell refinement were made using the Bruker SAINT<sup>+</sup> software package. The absorption correction was performed with SADABS<sup>42,43</sup>. The structure was solved by intrinsic phasing using SHELXT and refined by least squares on SHELXL under the Olex2<sup>44-46</sup> graphical interface. The crystallographic artwork representations were prepared using VESTA software<sup>47</sup>. The determined crystal structure belongs to the  $Fm\bar{3}m$  space group with  $a = 10.66180(10) \text{ \AA}$  as cell parameter, consistent with Ketelaar *et al.*<sup>48</sup>. The  $\text{Rb}_2\text{SnBr}_6$  crystals exhibited thicknesses ranging from 150  $\mu\text{m}$  to 250  $\mu\text{m}$ .

**Infrared Spectroscopy:** A Bruker Vertex 70 V Fourier-transform spectrometer acquired the infrared attenuated reflectance spectrum of a powdered sample. Data in the far-infrared region were collected using a mercury (Hg) lamp as the light source, while signal detection was carried out using DLaTGS pyroelectric detectors. The dataset was obtained through 256 scans and a spectral resolution of 2  $\text{cm}^{-1}$ .

**Diffuse UV-vis Reflectance Spectroscopy:** Room-temperature absorption spectra of grounded crystals were acquired using Diffuse Reflectance Spectroscopy (DRS) with a Shimadzu UV-2600 spectrophotometer equipped with an ISR-2600 Plus integrating

sphere, covering the 200–800 nm wavelength range. The reflectance data were converted into absorption spectra via the Kubelka-Munk function <sup>49</sup>.

**Photoluminescence (PL) and Raman Spectroscopies at Low-Temperatures:** PL spectra were collected using a T64000 Jobin–Yvon spectrometer equipped with an Olympus microscope and an LN<sub>2</sub>-cooled CCD to detect the emitted radiation of the sample in a single mode. The temperature-dependent PL spectra were excited with an external lamp (405 nm) using a long working distance plan-achromatic objective of 20x and keeping the sample in a vacuum inside a He-compressed closed-cycle cryostat. A Lakeshore 330 controller controlled the temperature with the precision of  $\pm 0.1$  K. Excitation intensity-dependent PL was recorded at 10 K using an Argon ion laser operating at a wavelength of 457 nm, digitally tuning the laser power and measuring its real value at laser focus with a Coherent LaserCheck Power Meter, keeping low intensities to avoid laser damage. The same temperature-dependent experimental setup was utilized to perform low-temperature Raman measurements of the. Each Raman and PL spectrum was deconvoluted for data analysis based on a sum of Voigt functions for Raman peaks and Gaussian functions for PL peaks using Fityk software <sup>50</sup>.

**Density Functional Theory (DFT) Calculations** First-principles calculations were performed using the Cambridge Serial Total Energy Package (CASTEP) code <sup>51</sup>, within the framework of Density Functional Theory (DFT) <sup>52,53</sup>. Norm-conserving pseudopotentials (NC) <sup>54</sup> were employed with valence electron configurations: 3d<sup>10</sup> 4s<sup>2</sup> 4p<sup>5</sup> (Br), 4s<sup>2</sup> 4p<sup>6</sup> 5s<sup>1</sup> (Rb), and 4d<sup>10</sup> 5s<sup>2</sup> 5p<sup>2</sup> (Sn). The exchange-correlation potential was described by the Generalized Gradient Approximation (GGA), while dispersive interactions were included via the Tkatchenko–Scheffler (TS) scheme. Structural optimizations utilized a 330 eV plane-wave cutoff with convergence criteria of  $\Delta E \leq 5 \times 10^{-6}$  eV/atom, forces  $< 0.01$  eV/Å, pressures  $< 0.02$  GPa, and atomic displacements  $< 5 \times 10^{-4}$  Å, consistent with prior DFT studies <sup>55–57</sup>. Optimization employed the Broyden–Fletcher–Goldfarb–Shanno (BFGS) <sup>58</sup>, and a Monkhorst–Pack 2x2x2 k-point grid for reciprocal-space integration. Geometry optimization results (GGA+TS<sub>330eV</sub>) agreed well with experimental values, displaying  $a^{DFT} = 10.5318$  Å, with a deviation of  $\sim 0.13$  Å (1.23 %). To address GGA bandgap underestimation, electronic and vibrational properties were calculated using the hybrid functional Heyd–Scuseria–Ernzerhof (HSE06) <sup>59–64</sup>. Parameters were consistent with vacancy-ordered perovskite

studies, such as  $\text{Cs}_2\text{BX}_6$  ( $\text{B} = \text{Sn}$  or  $\text{Ti}$ ;  $\text{X} = \text{Cl}$ ,  $\text{Br}$  or  $\text{I}$ )<sup>65</sup> calculations. The self-consistent field (SCF) convergence criteria included a total energy tolerance of  $0.5 \times 10^{-6}$  eV and eigenenergy tolerance of  $0.1406 \times 10^{-6}$  eV, achieved within three cycles at a  $2 \times 2 \times 2$  k-point grid.

### III. RESULTS

**Figure 1(a)** shows the crystalline structure of the 0D perovskite  $\text{Rb}_2\text{SnBr}_6$  at room conditions, which belongs to the  $Fm\bar{3}m$  space group. This structure is derived from the 3D  $\text{RbSnBr}_3$  perovskite<sup>48,66</sup> by withdrawing half of Sn atoms that occupy the  $[\text{SnBr}_6]^{2-}$  octahedra centers, with  $\text{Rb}^+$  ions embracing 12-fold coordination at sites among the  $[\text{SnBr}_6]^{2-}$  units. The measured Sn-Br bond length of 2.5938(4) Å is constant along all octahedra, indicating a lack of bond distortions in the  $[\text{SnBr}_6]^{2-}$  octahedron. **Table S1** (see Supporting Information) summarizes the crystal data and parameters from SCXRD data refinement.

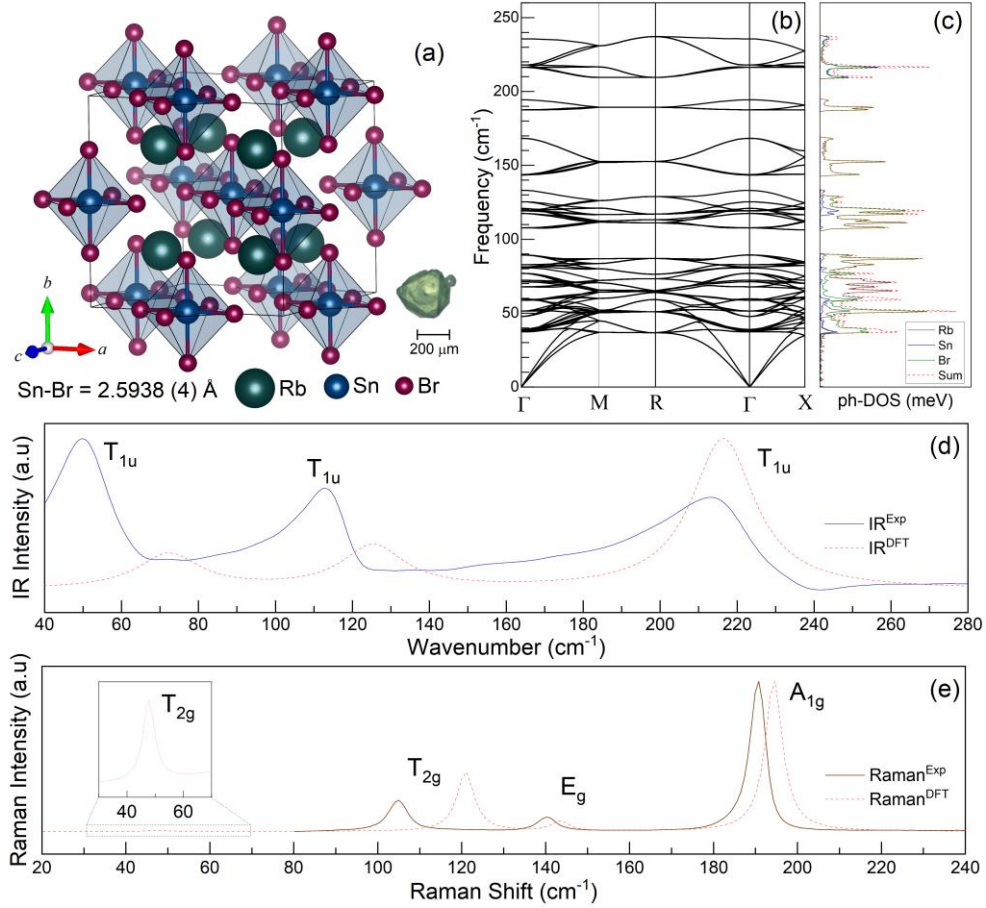


**Figure 1:** (a) Crystalline structure of  $\text{Rb}_2\text{SnBr}_6$  at room conditions with an inset showing one of the microcrystals synthesized in this work. (b) Calculated phonon dispersion across the whole Brillouin zone, (c) ph-DOS contribution for each element: black (Rb), blue (Sn), and green (Br). The dashed red line describes the ph-DOS sum. The observed and calculated optical modes are displayed in the normalized spectrum of (d) IR reflectance and (e) Raman spectroscopy.



The group theory with basis on the site occupation of  $Fm\bar{3}m$  space group from  $Rb_2SnBr_6$  predicts ten normal modes, which can be decomposed among the irreducible representation of the  $m\bar{3}m$  factor group as:  $\Gamma_M = A_{1g} \oplus E_g \oplus T_{2u} \oplus 2T_{2g} \oplus 4T_{1u} \oplus T_{1g}$ . Among these modes, those with symmetries  $T_{1g}$  and  $T_{2u}$  are silent, one with symmetry  $T_{1u}$  is acoustic, three with symmetry  $T_{1u}$  are IR active, while the modes with symmetries  $A_{1g}$ ,  $E_g$  and  $2T_{2g}$  are Raman active. **Figure 1(b)** displays the calculated phonon dispersion along high-symmetry points ( $\Gamma, M, R, X$ ) in the Brillouin zone. The vibrational frequencies span from 0 to 250  $cm^{-1}$ , with distinct separation of vibrational branches. The acoustic modes exhibit typical linear behavior near the  $\Gamma$ -point, with the longitudinal acoustic (LA) and transverse acoustic (TA) modes displaying moderate dispersion, reflecting the rigidity and isotropy of the crystal lattice <sup>67,68</sup>.

The optical branches show significant splitting due to the pronounced mass contrast between Rb and Sn/Br and the macroscopic electric field inherent to the polar nature of  $Rb_2SnBr_6$ , a behavior observed in  $CsBI_3$  ( $B = Pb, Sn$ ) <sup>69</sup>. **Figure 1(c)** highlights the phonon density of states (ph-DOS) contributions of Rb, Sn, and Br atoms to the vibrational modes. Low-frequency modes below 50  $cm^{-1}$  are primarily associated with the lattice vibrations dominated by the rattling motion of Rb atoms, as evidenced by a pronounced peak in the Rb-projected ph-DOS. Frequency modes (50–150  $cm^{-1}$ ) are attributed to bending vibrations of the  $[SnBr_6]^{2-}$  octahedra, with contributions from both Sn and Br atoms. LO and TO splitting are observed around this region, while high-frequency modes (above 150  $cm^{-1}$ ) are dominated by stretching vibrations of the Sn–Br bonds, which reveals relatively low dispersion.

The normalized Far-IR reflectance spectrum of  $Rb_2SnBr_6$  at room temperature, which is shown in **Figure 1(d)**, shows the three IR modes predicted from theory <sup>70</sup>: the highest wavenumber mode  $\nu_{as}(T_{1u})$  corresponds to asymmetric stretching of Sn-Br bonds, the intermediate wavenumber vibration  $\delta_{as}(T_{1u})$  represents the Br-Sn-Br asymmetric bending, and the lowest wavenumber mode  $\nu^L(T_{1u})$  is related to a lattice mode with out-of-phase displacements of  $[SnBr_6]^{2-}$  octahedra and  $Rb^+$  cations. To obtain the frequencies of TO and LO modes, we used the Kramers-Kronig relations <sup>71</sup> on the reflectance spectra to obtain the real  $Re(\epsilon)$  and imaginary  $Img(\epsilon)$  parts of the dielectric function  $\epsilon(\omega)$ . The TO modes correspond to peaks in  $Img(\epsilon)$ , whereas maxima in the

imaginary part of the inverse of the dielectric function  $-Img(1/\epsilon)$  represent the LO modes. Both  $Img(\epsilon)$  and  $-Img(1/\epsilon)$  are shown in **Figure S1** (see Supporting Information). The obtained wavenumber values of the LO and TO modes are listed in **Table S2**. To obtain the high-frequency dielectric constant  $\epsilon_\infty$ , we extrapolated  $Re(\epsilon)$  at high frequencies and estimated  $\epsilon_\infty = 3.71$ . The static dielectric constant  $\epsilon_s$  was calculated through the generalized Lyddane-Sachs-Teller relation <sup>71</sup>:

$$\frac{\epsilon_s}{\epsilon_\infty} = \prod_i \left( \frac{\omega_{LO,i}}{\omega_{TO,i}} \right)^2 \quad (1)$$

where  $\omega_{TO}$  and  $\omega_{LO}$  are the TO and LO frequencies, respectively. Using the experimental values of the TO and LO modes in **Equation 1**,  $\epsilon_s$  was evaluated as 7.57. These parameters are in accordance with previously reported theoretical values for isomorphous compounds  $Cs_2BX_4$  (B = Sn, Ti; X = Cl, Br, I) <sup>72</sup>.

**Figure 1(e)** presents the room-temperature Raman spectrum of  $Rb_2SnBr_6$  under 457 nm excitation wavelength (2.71 eV), which consists mainly of three intense peaks linked to modes of  $[SnBr_6]^{2-}$  vibrations that can be described, from lower to higher Raman shift, as follow <sup>70,73</sup>:  $\delta_{as}(T_{2g}) = 105 \text{ cm}^{-1}$  asymmetric bending of Br-Sn-Br bonds,  $\nu_{as}(E_g) = 140 \text{ cm}^{-1}$  asymmetric Sn-Br stretching and  $\nu_s(A_{1g}) = 191 \text{ cm}^{-1}$  symmetric stretching of Sn-Br. A fourth weak intensity peak at a higher Raman shift was assigned as the second-order mode of  $\nu_s(A_{1g})$ . The other  $\nu^L(T_{2g})$  Raman active mode, corresponding to vibrations of  $Rb^+$  cations within fixed  $[SnBr_6]^{2-}$  lattice framework, is supposed to be at Raman shift values lower than  $80 \text{ cm}^{-1}$  (out of measured range). This mode aligns with the low-intensity calculated Raman DFT phonon around  $50 \text{ cm}^{-1}$ . These observations confirm strong agreement between experimental and DFT-calculated Raman and IR modes, with all frequencies aligning with the calculated phonon dispersion and ph-DOS. Summarized values are provided in **Table S2**.

We performed low-temperature Raman spectroscopy to investigate possible structural phase transitions (SPT) or other anomalies in  $Rb_2SnBr_6$ . However, no substantial changes consistent with SPT or other anomalies were observed aside from expected thermal lattice anharmonicity accompanied by a narrowing of Raman peaks upon cooling, as shown in **Figure S2** (see Supporting Information). The changes in Raman shift modes from room-temperature to low-temperatures were notably small, with

the highest difference less than  $5 \text{ cm}^{-1}$  (0.6 meV) for the  $\nu_s(A_{1g})$ , showing that the cubic structure and bonding strength persist at lower temperatures<sup>33</sup>. This is expected because the vacancy-ordered structure maintains the configuration of isolated octahedra, preventing phase transitions induced by tilting corner-sharing octahedra, commonly occurring in perovskites during lattice contraction<sup>74,75</sup>.

**Figure 2(a)** presents the calculated electronic band structure of  $\text{Rb}_2\text{SnBr}_6$  by DFT. These 0D MHPs exhibit a direct electronic transition at the  $\Gamma$ -point (3.11 eV). From the density of states (DOS) of the electronic band structure shown in **Figure 2(b)**, the valence band maximum (VBM) and conduction band minimum (CBM) are derived from the splitting of  $[\text{SnBr}_6]^{2-}$  octahedra molecular orbital, with a nonbonding Br  $p$ -state at the VBM, and single bonding Sn-Br ( $s$ - $p$ ) state at the CBM, similar to  $\text{Cs}_2\text{SnBr}_6$ <sup>36,72</sup>. The CBM has a gradient band edge from the mixing and delocalization of Sn  $s$  and Br  $p$  states, while the VBM presents less dispersive features from the fully oxidized  $\text{Sn}^{4+}$ , unlike conventional 3D tin halide with partially oxidized  $\text{Sn}^{2+}$  and filled valence subshell<sup>65</sup>, indicating the presence of light electrons and heavy holes as can be seen from the effective masses  $\overline{m}_e$  and  $\overline{m}_h$  of electron and hole, respectively, with values of  $\overline{m}_e = 0.22m_0$  and  $\overline{m}_h = 1.3m_0$  where  $m_0$  is the electron rest mass. To estimate the free-exciton binding energy  $E_{ex}$ , we used the Wannier-Mott model based on dielectric screening and electronic band structure given by<sup>76</sup>

$$E_{ex} = \frac{\mu}{m_0 \epsilon_\infty^2} Ry \quad (2)$$

where  $\mu = (\overline{m}_e \times \overline{m}_h) / (\overline{m}_e + \overline{m}_h)$  is the reduced mass of the electron-hole pair, and  $Ry$  is the Rydberg energy (13.6 eV). We found a large value for  $E_{ex}$  of 186 meV from this model, which suggests strong electron-hole interactions in  $\text{Rb}_2\text{SnBr}_6$  that can be associated with reduced dimensionality compared to 3D halide counterparts that lowers dielectric screening, thus enhancing the Coulomb potential of electron-hole pair that stabilizes the exciton against collisions with phonons<sup>77</sup>. The value of  $E_{ex}$  is consistent with prior reports on vacancy-ordered perovskites<sup>35</sup>.

To measure the optical bandgap of  $\text{Rb}_2\text{SnBr}_6$ , we conducted UV-Vis DRS in polycrystalline samples at room temperature with the obtained reflectance spectrum  $R(\omega)$  converted to absorbance units using the Kubelka-Monk function  $F(R)$  as shown in

**Figure 2(c).** We can see that the optical absorption edge is around 450 nm. We estimated the energy bandgap by extrapolating the linear direct-Tauc plot <sup>78</sup>, given by  $[F(R)E]^2 \propto (E - E_g)$  where  $E$  is the energy and  $E_g$  stands for the direct energy bandgap, obtaining  $E_g = 2.960 (1) \text{ eV}$ . This experimental bandgap aligns remarkably well with the theoretical bandgap obtained through DFT calculations and it is in good agreement with other isomorphous perovskites <sup>79–81</sup>.

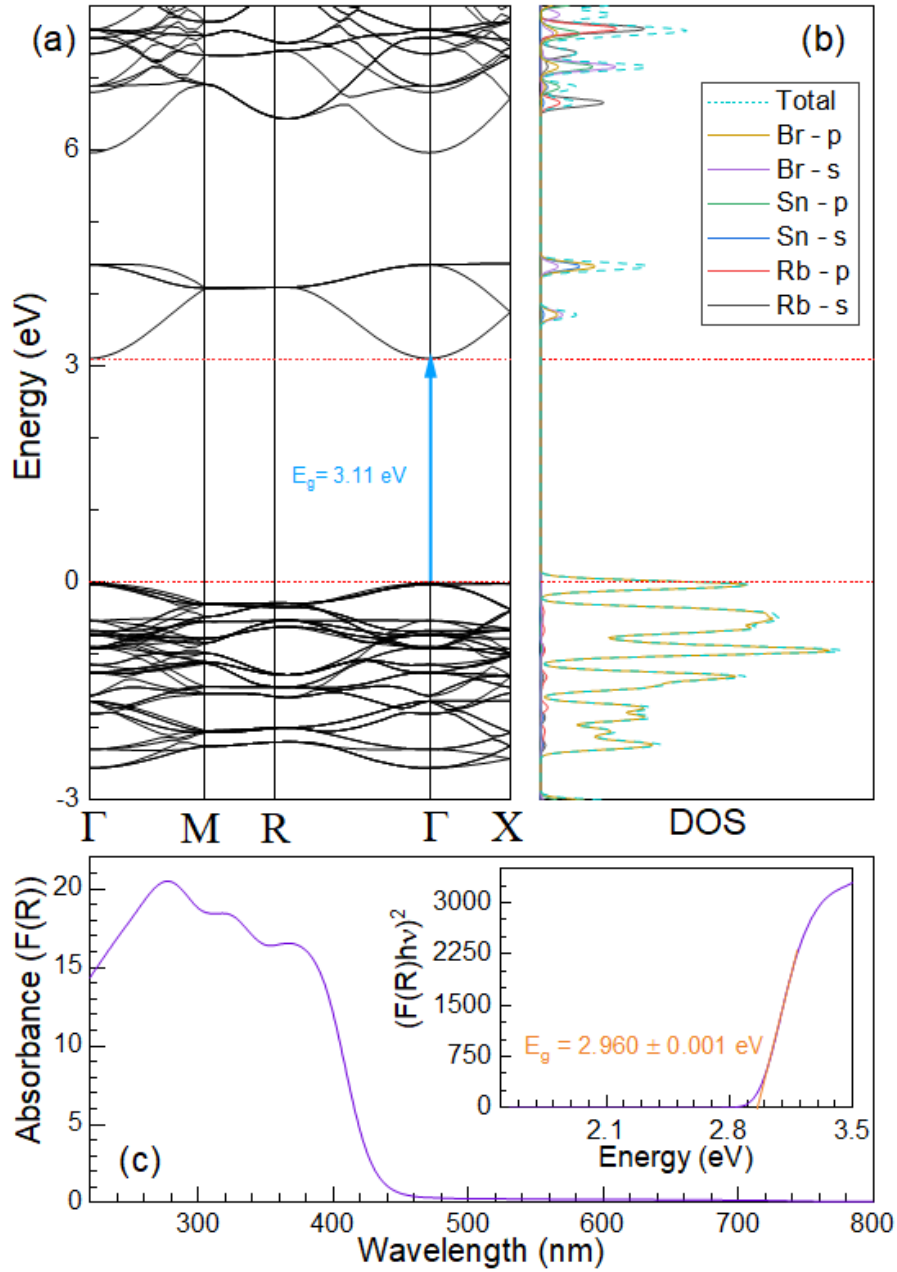


**Figure 2:** (a) Electronic band structure, (b) density of states (DOS), and (c) normalized absorbance spectrum of  $\text{Rb}_2\text{SnBr}_6$ . The inset shows the direct-Tauc plot. The calculated bandgap (3.11 eV) is consistent with the experimental optical bandgap (2.96 eV).

The PL spectrum of  $\text{Rb}_2\text{SnBr}_6$  at 10 K under UV excitation (3.06 eV) showed in **Figure 3(a)** revealed a broad emission around 1.93 eV (642 nm) and a full width at half maximum (FWHM) of 202 meV, which can be modeled by a Gaussian peak. Such broadband and large Stokes shift energy is usually found in low-dimensional halide perovskites<sup>79,82,83</sup>. They are usually attributed to a wide distribution of states inside the bandgap that behave as traps to charge carriers where below-gap photons can be emitted<sup>76,84</sup> or to STE luminescence where strong EPC plays a crucial role creating polarons from lattice distortions that bind charge carries of an exciton to the lattice (self-trapping) at in-gap energy levels with subsequent phonon-assisted radiative emission from exciton recombination<sup>76,85,86</sup>.

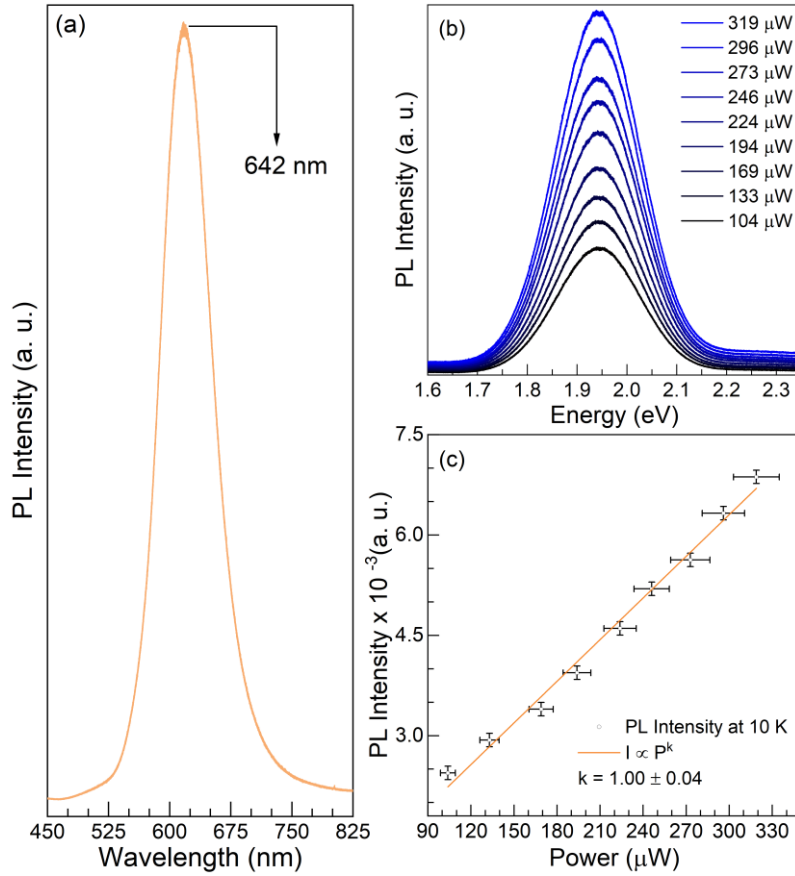


**Figure 3:** (a) PL spectrum at 10 K of  $\text{Rb}_2\text{SnBr}_6$ . (b) PL emission dependence of  $\text{Rb}_2\text{SnBr}_6$  PL at 10 K on excitation power. (c) A plot of PL intensity vs power was obtained from (b).

To further verify the origin of the  $\text{Rb}_2\text{SnBr}_6$  emission band, we performed the PL intensity dependence on excitation power at 10 K, as illustrated in **Figure 3(b)**. An increase in intensity and a small redshift of 1 meV on the PL peak was observed while

the excitation power increased from 104  $\mu\text{W}$  to 319  $\mu\text{W}$ . The general relation of PL intensity  $I$  and excitation power  $P$  is described as  $I \propto P^k$ , where the exponent  $k$  lies on the ranges  $0 < k < 1$  for free-to-bound transitions or donor-acceptor pairs (DAP) recombination and  $1 < k < 2$  for excitonic emission<sup>87</sup>. Excitation energies close to the bandgap energy tend to result in a linear relation between  $I$  and  $P$  for the excitonic recombination process that agrees with our data, as seen in **Figure 3(c)**, which shows the plot of  $I$  vs  $P$ , yielding  $k = 1.00 \pm 0.04$ . The redshift behavior contrasts with the characteristic blueshift of DAP recombination, which excludes this possibility of emission mechanism<sup>76</sup>.

Additionally, free-to-bound transitions are identified as acceptor or donor levels that bind carriers and become ionized at higher temperatures, leading to emission bands from free carriers<sup>32,88</sup>. That is not observed on the temperature-dependent PL spectra in **Figure 4(a)** once the peak energy and intensity monotonically decrease from 10 K until its quenching around 180 K with no other radiative emission bands detected. Thus, free-to-bound recombination should not be the mechanism of luminescence found in our results. In this way, we suggest that exciton recombination is responsible for PL emission of  $\text{Rb}_2\text{SnBr}_6$ .

The PL emission color, under UV excitation upon increasing temperature from 10 K, changed from orange to light-yellow until 180 K, where no PL emission could be detected (see the inset of **Figure 4(a)** that shows the dependence of PL peak energy with temperature and the CIE plot in **Figure S3** with chromaticity coordinates in **Table S3**). Moreover, the PL thermal quenching behavior was modeled considering the integrated PL intensity  $I_{PL}(T)$  as a function of the temperature  $T$  using the Arrhenius equation<sup>89,90</sup> given by

$$I_{PL}(T) = \frac{I_0}{1 + Ae^{\frac{-E_a}{k_B T}}} \quad (3)$$

where  $k_B$  is the Boltzmann constant,  $I_0$  stands for zero-temperature integrated intensity,  $A$  corresponds to the density of radiative recombination centers, and  $E_a$  relates to the activation energy for thermal quenching. **Equation 3** fully agreed with our data, as it is shown in **Figure 4(b)**, estimating an activation energy  $E_a = 16.7 \pm 0.7$  meV, close to the quenching temperature of 180 K ( $\approx 16$  meV). The absence of emission beyond 180 K

suggests that the calculated activation energy is associated with the nonradiative recombination process.

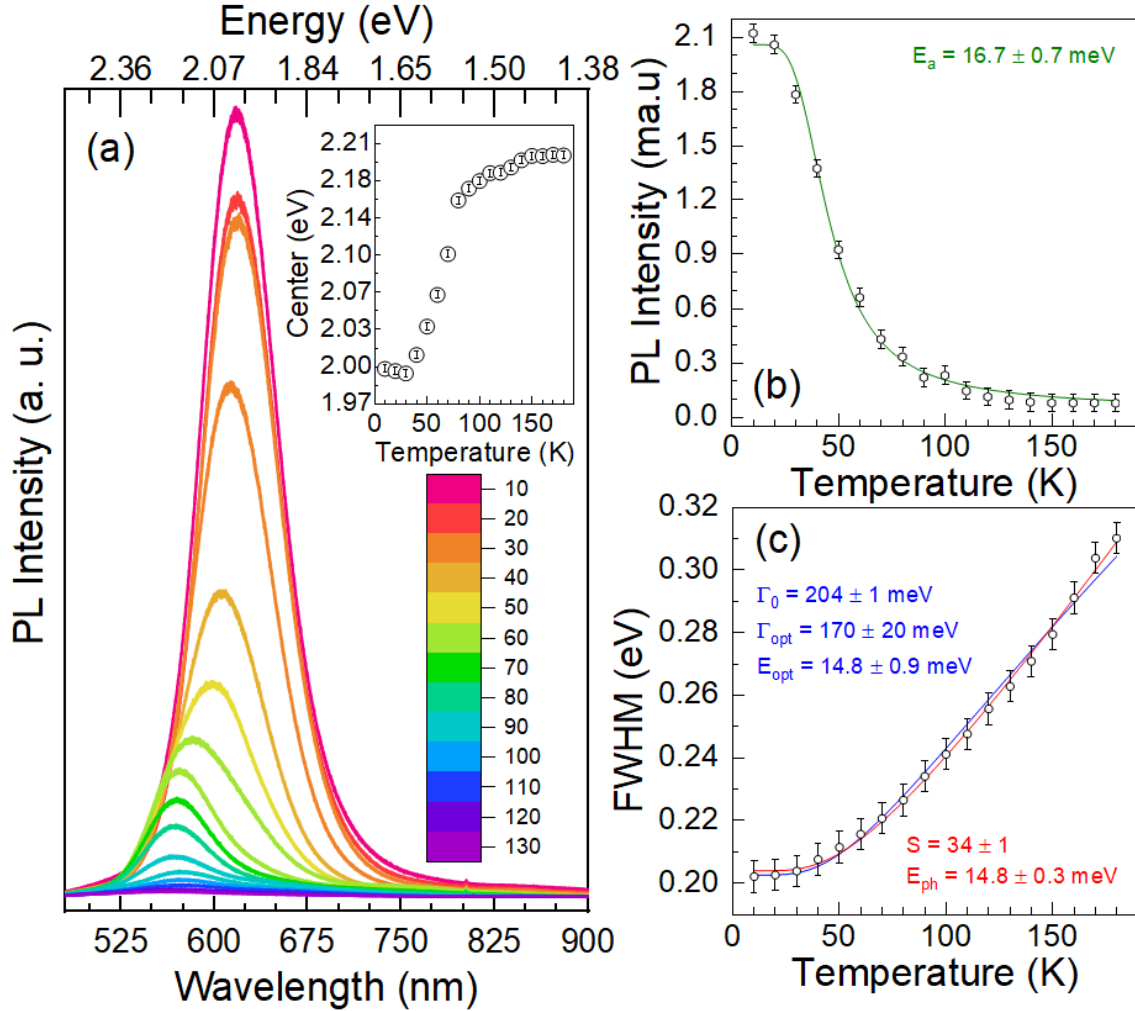


**Figure 4:** (a) Temperature-dependent PL spectra of  $\text{Rb}_2\text{SnBr}_6$ . The inset shows the temperature dependence of peak energy. (b) Integrated PL intensity vs temperature fitted with **Equation 2**. (c) PL FWHM vs temperature analyzed by **Equation 3** (solid blue line) and **Equation 4** (solid red line).

To evaluate the EPC strength involved in the luminescence phenomena of  $\text{Rb}_2\text{SnBr}_6$ , we investigated the temperature dependence of PL FWHM presented in **Figure 4(c)** based on two perspectives. The first model used to examine the PL linewidth was elaborated by Rudin et al.<sup>91</sup> and concerns different contributions to PL broadening on temperature, which can be represented as the sum of functional dependencies into FWHM:

$$FWHM(T) = \Gamma_0 + \Gamma_{ac}T + \frac{\Gamma_{LO}}{e^{\frac{E_{LO}}{k_B T}} - 1} + \Gamma_{imp}e^{\frac{-E_{imp}}{k_B T}} \quad (4)$$

In the **Equation 4**, the first term  $\Gamma_0$  is the inhomogeneous broadening arising from scattering due to lattice disorder <sup>24</sup>; the second term  $\Gamma_{ac}$  the term represents the homogeneous broadening from the coupling between excitons and acoustic phonons through deformation potential scattering where lattice distortions modify the electronic band structure <sup>92</sup>; the third term  $\Gamma_{LO}$  stands for the homogenous broadening contribution of LO phonons of energy  $E_{LO}$  via long-range Fröhlich interactions, which is proportional to the occupation number of phonons given by Bose-Einstein distribution  $1/(e^{\frac{E_{LO}}{k_B T}} - 1)$  and emerges from the interplay between the macroscopic electric field induced by LO vibrations and exciton's charge carriers <sup>33</sup>; the last term  $\Gamma_{imp}$  accounts for scattering from ionized impurities with mean binding energy  $E_{imp}$  <sup>93</sup>.

Based on our previous analysis about the PL intensity dependence on excitation power that excluded DAP or free-to-bound recombination process and the linear increase of FWHM experimental data as it approximates the quenching temperature, which does not agree with the asymptotic behavior expected from the exponential term associated with ionized impurities, we assumed  $\Gamma_{imp} = 0$ . At the low-temperature range, the optical phonon contributions from the Bose-Einstein distribution function give a gradient of zero in the regime of  $E_{LO} < k_B T$ . However, on a typically observable range of temperature, as achieved in this work, acoustic phonons have significantly lower energies than  $k_B T$  and a non-zero gradient of  $\Gamma_{ac}$  is predicted as  $T$  approaches zero <sup>24</sup>. Observing the FWHM dependence on temperature, we see that the gradient tends to vanish for the lowest temperatures, indicating negligible contribution from acoustic modes ( $\Gamma_{ac} \approx 0$ ) which was further verified with the fit convergence when  $\Gamma_{ac} \rightarrow 0$ . Therefore, we concluded that Fröhlich interactions through LO phonons play a major role in PL broadening temperature dependence.

Thus, fitting the PL FWHM with **Equation 4** considering only the coupling between excitons and LO phonons from the Fröhlich mechanism and the temperature-independent inhomogeneous broadening, we obtain  $\Gamma_0 = 204 \pm 1$  meV,  $\Gamma_{LO} = 170 \pm 20$  meV and  $E_{LO} = 14.8 \pm 0.9$  meV. The energy  $E_{LO}$  is closely related with  $\delta_{as}(T_{1u})$  LO phonon mode at  $120 \text{ cm}^{-1}$  ( $\approx 15$  meV) obtained by IR analysis at room temperature, which



suggests that long-range Fröhlich interactions mediated by LO phonons are the dominant mechanisms of EPC that impact PL broadening, that is commonly expected in polar semiconductors as is the case for  $\text{Rb}_2\text{SnBr}_6$ <sup>10,94</sup>. In the present case, the  $\Gamma_{LO}$  parameter measures the strength of electron-phonon coupling that is notably higher than in 3D perovskites<sup>24,95</sup>, shedding light on the strong strength of EPC in low-dimensional perovskite compounds.

The second model used to evaluate the EPC strength was developed by Toyozawa<sup>96,97</sup> employing a configuration coordinate model where the mean number of phonons with effective energy  $E_{ph}$  emitted after exciton recombination is described by the Huang-Rhys factor  $S$ <sup>29</sup> in the form of

$$FWHM(T) = 2.36\sqrt{S}E_{ph}\sqrt{\coth\left(\frac{E_{ph}}{2k_B T}\right)} \quad (5)$$

Here, the value of  $S$  determines the regime of EPC. Generally,  $S \gg 1$  implies a strong coupling regime<sup>76</sup>. In Toyozawa's theory, the case of strong electron/exciton-phonon coupling would lead to a Gaussian shape of PL linewidth rather than a Lorentzian one, that happens in the weak couple regime<sup>85</sup>, which is consistent with our findings. The temperature-dependent FWHM fitted with **Equation 5** yielded  $E_{ph} = 14.8 \pm 0.3$  meV and  $S = 34 \pm 1$ . The effective phonon energy matches with the LO phonon energy  $E_{LO}$  of the  $\delta_{as}(T_{1u})$  mode previously found with Rudin's model, supporting that the EPC of  $\text{Rb}_2\text{SnBr}_6$  arises from Fröhlich interactions with LO phonons. The strong EPC revealed by the Huang-Rhys factor agrees with the high value obtained from  $\Gamma_{LO}$  and is compatible with the assumption of exciton self-trapping underlying the below-gap broad luminescence from STE as observed in many halide perovskites available in the literature<sup>31,32,79,98</sup>.

In the Fröhlich theory, the polaron formation arises from the interactions between carriers and LO phonons, and the coupling strength of this carrier-vibration relation is determined by the Fröhlich parameter  $\alpha$  that is defined as

$$\alpha = \frac{e^2}{4\pi\epsilon_0\hbar}\left(\frac{1}{\epsilon_\infty} - \frac{1}{\epsilon_s}\right)\sqrt{\frac{\bar{m}}{2\hbar\omega}} \quad (6)$$

where  $e$  is the electron charge,  $\epsilon_0$  is the vacuum permittivity,  $\hbar$  is the reduced Planck constant,  $\omega$  is the LO phonon frequency, and  $\bar{m}$  is the effective mass of the electron or hole. Using the first-principles calculated effective masses as well as the experimental values for  $\hbar\omega$  (LO phonon energy),  $\epsilon_\infty$  and  $\epsilon_s$ , **Equation 6** yielded Fröhlich parameters of 1.94 and 4.73 for the electron and hole, respectively. Although  $\alpha$  for the electrons is the same range of  $\approx 2$ <sup>27,94</sup> for conventional 3D halide perovskites, we note that the hole-phonon coupling is well above this range and more than twice the value for the electrons. This is a direct consequence of the heavy hole mass compared to the electron found through DFT calculations. Upon hole interactions with surrounding lattice, its mass is further increased by the hole-polaron mass<sup>99</sup>  $\bar{m}_{hp} \approx \left(1 + \frac{\alpha}{6} + \frac{\alpha^2}{40}\right) \bar{m}_h = 3.05m_0$  that aid hole localization and consequently exciton trapping by its positive carrier. Thus, we proposed that STE formation in  $\text{Rb}_2\text{SnBr}_6$  is mediated by hole localization upon Fröhlich interactions with the lattice vibration. This kind of exciton formation has been observed in organic and molecular crystals<sup>100</sup>, and total inorganic salts such as  $\text{AgCl}$ <sup>76,101</sup>.

The above results about the strong EPC of low-dimensional  $\text{Rb}_2\text{SnBr}_6$  compared with 3D halide perovskites can be interpreted in terms of the  $[\text{BX}_6]$  octahedra that are most responsible for the electronic and optical properties of many perovskite materials<sup>2,102,103</sup>: while in 3D perovskites the octahedra are surrounded by a corner-sharing framework, isolated  $[\text{BX}_6]$  octahedra configuration of 0D perovskites possess more degrees of freedom and hence are easily distorted upon interaction between exciton's charge carriers (in the present case, the hole) and octahedra vibrations creating polarons that are dynamically related to LO phonons due the polar nature of the perovskites<sup>21,104</sup>. Thus, the enhancement of EPC promotes exciton trapping and STE formation, which leads to a broad luminescence with large Stokes shift energy, as shown by our findings and data analysis.

## IV. CONCLUSIONS

We investigated the electron-phonon coupling in 0D  $\text{Rb}_2\text{SnBr}_6$  microcrystals, analyzing their structural, vibrational, and optical properties through several experimental techniques and theoretical calculations. Specifically, single crystal X ray diffraction revealed a cubic symmetry in  $Fm\bar{3}m$  space group with a direct energy bandgap  $E_g = 2.9602(9) \text{ eV}$  in the UV-Vis range obtained by diffuse reflection spectroscopy. Infrared and Raman spectroscopies showed the main vibrational modes associated with bending and stretching of  $[\text{SnBr}_6]^{2-}$  octahedra, and low-temperature Raman analyses provided no evidence of any SPT down to 10 K. DFT results were very consistent with the vibrational and optical properties found at room temperature. Low-temperature photoluminescence (PL) spectrum indicated a broad emission with large Stokes shift energy consistent with excitonic self-trapping, as the power and temperature-dependent PL pointed out. The EPC was evaluated upon the PL linewidth broadening temperature dependence based on two perspectives where charge carries interplay with Br-Sn-Br asymmetric bending of LO phonons mediated by Fröhlich interactions were the main mechanism responsible for the PL broadening through phonon-assisted radiative emission. Strong EPC was elucidated by the Huang-Rhys factor  $S = 34 \pm 1$  coherent with STE emission commonly found in low-dimensional perovskites. The Fröhlich parameter  $\alpha$  found through experimental data, and theoretical calculations pointed out the main contributions of hole localization by large hole-polaron mass in STE formation. Our work provides a fundamental understanding of the correspondence between vibrational and optoelectronic properties of  $\text{Rb}_2\text{SnBr}_6$ , guiding its applications such as light-harvesting devices.

## **AUTHOR CONTRIBUTIONS**

C. C. S. S. and J. S. R. H. conceptualized the project. C. C. S. S. wrote the original draft. Experimental work was conducted by C. C. S. S., J. S. R. H., V. S. N., and M. A. P. G., performing the single crystal x-ray diffraction, diffuse reflectance spectroscopy, Raman spectroscopy, IR spectroscopy, and photoluminescence. B. P. S performed the first-principles calculations. The data analysis was conducted by C. C. S. S., and J. S. R. H. Supervision, resources, and funding acquisition were acquired by C. W. A. P. and A. P. A. All authors participated in reviewing and interpreting the results.

## ACKNOWLEDGEMENTS

This investigation was financed in part by Fundação Cearense de Apoio ao Desenvolvimento Científico e Tecnológico (UNI-0210-00047.01.00/23, 07548003/2023), the Conselho Nacional de Pesquisa e Desenvolvimento do Brasil (CNPq – Projetos 407956/2022-0, 407954/2022-8, 406322/2022-8, 310353/2023-8), and Coordenação de Aperfeiçoamento de Pessoal de Nível Superior do Brasil (CAPES) - Finance Code 001 (CAPES – Projeto 88887.669776/2022-00). The authors would like to thank Prof. Tiago Pinheiro Braga from the Physical–Chemistry Department of the Federal University of Rio Grande do Norte and the NPAD/UFRN for the computational resources provided. Additional calculations were conducted using the resources of the Centro Nacional de Processamento de Alto Desempenho in São Paulo (CENAPAD-SP), Project 823.

## V. REFERENCES

- (1) Zhang, W.; Eperon, G. E.; Snaith, H. J. Metal Halide Perovskites for Energy Applications. *Nat Energy* **2016**, *1* (6), 16048. <https://doi.org/10.1038/nenergy.2016.48>.
- (2) Dong, H.; Ran, C.; Gao, W.; Li, M.; Xia, Y.; Huang, W. Metal Halide Perovskite for Next-Generation Optoelectronics: Progresses and Prospects. *eLight* **2023**, *3* (1), 3. <https://doi.org/10.1186/s43593-022-00033-z>.
- (3) Liu, X.-K.; Xu, W.; Bai, S.; Jin, Y.; Wang, J.; Friend, R. H.; Gao, F. Metal Halide Perovskites for Light-Emitting Diodes. *Nat Mater* **2021**, *20* (1), 10–21. <https://doi.org/10.1038/s41563-020-0784-7>.
- (4) Hong, K.; Le, Q. Van; Kim, S. Y.; Jang, H. W. Low-Dimensional Halide Perovskites: Review and Issues. *J Mater Chem C Mater* **2018**, *6* (9), 2189–2209. <https://doi.org/10.1039/C7TC05658C>.
- (5) Han, Y.; Yue, S.; Cui, B. Low-Dimensional Metal Halide Perovskite Crystal Materials: Structure Strategies and Luminescence Applications. *Advanced Science* **2021**, *8* (15). <https://doi.org/10.1002/advs.202004805>.
- (6) Li, S.; Li, X.; Kocoj, C. A.; Ji, X.; Yuan, S.; Macropulos, E. C.; Stoumpos, C. C.; Xia, F.; Mao, L.; Kanatzidis, M. G.; Guo, P. Ultrafast Excitonic Response in Two-Dimensional Hybrid Perovskites Driven by Intense Midinfrared Pulses. *Phys Rev Lett* **2022**, *129* (17), 177401. <https://doi.org/10.1103/PhysRevLett.129.177401>.
- (7) Zhou, Q.; Li, W.; Xiao, J.; Li, A.; Han, X. Low-Dimensional Metal Halide for High Performance Scintillators. *Adv Funct Mater* **2024**, *34* (38). <https://doi.org/10.1002/adfm.202402902>.
- (8) Chen, C.; Xu, J.; Wang, X.; Palgrave, R. G. Two-Dimensional Complex Metal Halides: Influence of Restricted Dimensionality on Functional Properties. *J Mater Chem A Mater* **2024**, *12* (9), 5055–5079. <https://doi.org/10.1039/D3TA04742C>.
- (9) Nonato, A.; Rodríguez-Hernández, J. S.; Abreu, D. S.; Soares, C. C. S.; Gómez, M. A. P.; García-Fernández, A.; Señarís-Rodríguez, M. A.; Andújar, M. S.; Ayala, A. P.; Silva, R. X. da; Paschoal, C. W. A. Strong Electron–Phonon Coupling and Lattice Dynamics in One-Dimensional [(CH<sub>3</sub>)<sub>2</sub>NH<sub>2</sub>]PbI<sub>3</sub> Hybrid Perovskite. *Chemistry of Materials* **2025**, *37* (3), 1013–1026. <https://doi.org/10.1021/acs.chemmater.4c02670>.
- (10) Yamada, Y.; Kanemitsu, Y. Electron-Phonon Interactions in Halide Perovskites. *NPG Asia Mater* **2022**, *14* (1), 48. <https://doi.org/10.1038/s41427-022-00394-4>.

- (11) Nandi, P.; Shin, S.; Park, H.; In, Y.; Amornkitbamrung, U.; Jeong, H. J.; Kwon, S. J.; Shin, H. Large and Small Polarons in Highly Efficient and Stable Organic-Inorganic Lead Halide Perovskite Solar Cells: A Review. *Solar RRL* **2024**, *8* (14). <https://doi.org/10.1002/solr.202400364>.
- (12) Geuchies, J. J.; Klarbring, J.; Virgilio, L. Di; Fu, S.; Qu, S.; Liu, G.; Wang, H.; Frost, J. M.; Walsh, A.; Bonn, M.; Kim, H. Anisotropic Electron–Phonon Interactions in 2D Lead-Halide Perovskites. *Nano Lett* **2024**, *24* (28), 8642–8649. <https://doi.org/10.1021/acs.nanolett.4c01905>.
- (13) Giustino, F. Electron-Phonon Interactions from First Principles. *Rev Mod Phys* **2017**, *89* (1), 015003. <https://doi.org/10.1103/RevModPhys.89.015003>.
- (14) Zhu, X.; Egger, D. A. Effect of Overdamped Phonons on the Fundamental Band Gap of Perovskites. *Phys Rev Lett* **2025**, *134* (1), 016403. <https://doi.org/10.1103/PhysRevLett.134.016403>.
- (15) Zhu, C.; Jin, J.; Wang, Z.; Xu, Z.; Folgueras, M. C.; Jiang, Y.; Uzundal, C. B.; Le, H. K. D.; Wang, F.; Zheng, X. (Rayne); Yang, P. Supramolecular Assembly of Blue and Green Halide Perovskites with Near-Unity Photoluminescence. *Science (1979)* **2024**, *383* (6678), 86–93. <https://doi.org/10.1126/science.adi4196>.
- (16) Qu, S.; Sharma, V. K.; Geuchies, J. J.; Grechko, M.; Bonn, M.; Pientka, F.; Kim, H. Mode-Resolved, Non-Local Electron–Phonon Coupling in Two-Dimensional Spectroscopy. *Nat Phys* **2025**. <https://doi.org/10.1038/s41567-025-02861-5>.
- (17) Franchini, C.; Reticcioli, M.; Setvin, M.; Diebold, U. Polarons in Materials. *Nat Rev Mater* **2021**, *6* (7), 560–586. <https://doi.org/10.1038/s41578-021-00289-w>.
- (18) Miyata, K.; Meggiolaro, D.; Trinh, M. T.; Joshi, P. P.; Mosconi, E.; Jones, S. C.; De Angelis, F.; Zhu, X.-Y. Large Polarons in Lead Halide Perovskites. *Sci Adv* **2017**, *3* (8). <https://doi.org/10.1126/sciadv.1701217>.
- (19) Lee, W.; Alvertis, A. M.; Li, Z.; Louie, S. G.; Filip, M. R.; Neaton, J. B.; Kioupakis, E. Phonon Screening of Excitons in Atomically Thin Semiconductors. *Phys Rev Lett* **2024**, *133* (20), 206901. <https://doi.org/10.1103/PhysRevLett.133.206901>.
- (20) Filip, M. R.; Haber, J. B.; Neaton, J. B. Phonon Screening of Excitons in Semiconductors: Halide Perovskites and Beyond. *Phys Rev Lett* **2021**, *127* (6), 067401. <https://doi.org/10.1103/PhysRevLett.127.067401>.

- (21) Han, Y.; Cheng, X.; Cui, B.-B. Factors Influencing Self-Trapped Exciton Emission of Low-Dimensional Metal Halides. *Mater Adv* **2023**, *4* (2), 355–373. <https://doi.org/10.1039/D2MA00676F>.
- (22) Li, S.; Luo, J.; Liu, J.; Tang, J. Self-Trapped Excitons in All-Inorganic Halide Perovskites: Fundamentals, Status, and Potential Applications. *J Phys Chem Lett* **2019**, *10* (8), 1999–2007. <https://doi.org/10.1021/acs.jpcclett.8b03604>.
- (23) Xu, K.-X.; Lai, J.-M.; Gao, Y.-F.; Song, F.; Sun, Y.-J.; Tan, P.-H.; Zhang, J. High-Order Raman Scattering Mediated by Self-Trapped Exciton in Halide Double Perovskite. *Phys Rev B* **2022**, *106* (8), 085205. <https://doi.org/10.1103/PhysRevB.106.085205>.
- (24) Wright, A. D.; Verdi, C.; Milot, R. L.; Eperon, G. E.; Pérez-Osorio, M. A.; Snaith, H. J.; Giustino, F.; Johnston, M. B.; Herz, L. M. Electron–Phonon Coupling in Hybrid Lead Halide Perovskites. *Nat Commun* **2016**, *7* (1), 11755. <https://doi.org/10.1038/ncomms11755>.
- (25) Puppini, M.; Polishchuk, S.; Colonna, N.; Crepaldi, A.; Dirin, D. N.; Nazarenko, O.; De Gennaro, R.; Gatti, G.; Roth, S.; Barillot, T.; Poletto, L.; Xian, R. P.; Rettig, L.; Wolf, M.; Ernstorfer, R.; Kovalenko, M. V.; Marzari, N.; Grioni, M.; Chergui, M. Evidence of Large Polarons in Photoemission Band Mapping of the Perovskite Semiconductor CsPbBr<sub>3</sub>. *Phys Rev Lett* **2020**, *124* (20), 206402. <https://doi.org/10.1103/PhysRevLett.124.206402>.
- (26) Schlipf, M.; Poncé, S.; Giustino, F. Carrier Lifetimes and Polaronic Mass Enhancement in the Hybrid Halide Perovskite CH<sub>3</sub>NH<sub>3</sub>PbI<sub>3</sub> from Multiphonon Fröhlich Coupling. *Phys Rev Lett* **2018**, *121* (8), 086402. <https://doi.org/10.1103/PhysRevLett.121.086402>.
- (27) Frost, J. M. Calculating Polaron Mobility in Halide Perovskites. *Phys Rev B* **2017**, *96* (19), 195202. <https://doi.org/10.1103/PhysRevB.96.195202>.
- (28) Yazdani, N.; Bodnarchuk, M. I.; Bertolotti, F.; Masciocchi, N.; Fureraaj, I.; Guzelturk, B.; Cotts, B. L.; Zajac, M.; Rainò, G.; Jansen, M.; Boehme, S. C.; Yarema, M.; Lin, M.-F.; Kozina, M.; Reid, A.; Shen, X.; Weathersby, S.; Wang, X.; Vauthey, E.; Guagliardi, A.; Kovalenko, M. V.; Wood, V.; Lindenberg, A. M. Coupling to Octahedral Tilts in Halide Perovskite Nanocrystals Induces Phonon-Mediated Attractive Interactions between Excitons. *Nat Phys* **2024**, *20* (1), 47–53. <https://doi.org/10.1038/s41567-023-02253-7>.
- (29) de Jong, M.; Seijo, L.; Meijerink, A.; Rabouw, F. T. Resolving the Ambiguity in the Relation between Stokes Shift and Huang–Rhys Parameter. *Physical Chemistry Chemical Physics* **2015**, *17* (26), 16959–16969. <https://doi.org/10.1039/C5CP02093J>.



- (30) Hazra, V.; Mandal, A.; Bhattacharyya, S. Optoelectronic Insights of Lead-Free Layered Halide Perovskites. *Chem Sci* **2024**, *15* (20), 7374–7393. <https://doi.org/10.1039/D4SC01429D>.
- (31) Luo, H.; Guo, S.; Zhang, Y.; Bu, K.; Lin, H.; Wang, Y.; Yin, Y.; Zhang, D.; Jin, S.; Zhang, W.; Yang, W.; Ma, B.; Lü, X. Regulating Exciton–Phonon Coupling to Achieve a Near-Unity Photoluminescence Quantum Yield in One-Dimensional Hybrid Metal Halides. *Advanced Science* **2021**, *8* (14). <https://doi.org/10.1002/advs.202100786>.
- (32) McCall, K. M.; Stoumpos, C. C.; Kostina, S. S.; Kanatzidis, M. G.; Wessels, B. W. Strong Electron–Phonon Coupling and Self-Trapped Excitons in the Defect Halide Perovskites  $A_3M_2I_9$  ( $A = \text{Cs, Rb}$ ;  $M = \text{Bi, Sb}$ ). *Chemistry of Materials* **2017**, *29* (9), 4129–4145. <https://doi.org/10.1021/acs.chemmater.7b01184>.
- (33) Steele, J. A.; Puech, P.; Keshavarz, M.; Yang, R.; Banerjee, S.; Debroye, E.; Kim, C. W.; Yuan, H.; Heo, N. H.; Vanacken, J.; Walsh, A.; Hofkens, J.; Roeffaers, M. B. J. Giant Electron–Phonon Coupling and Deep Conduction Band Resonance in Metal Halide Double Perovskite. *ACS Nano* **2018**, *12* (8), 8081–8090. <https://doi.org/10.1021/acsnano.8b02936>.
- (34) Krahne, R.; Schleusener, A.; Faraji, M.; Li, L.-H.; Lin, M.-L.; Tan, P.-H. Phonon Directionality Impacts Electron–Phonon Coupling and Polarization of the Band-Edge Emission in Two-Dimensional Metal Halide Perovskites. *Nano Lett* **2024**, *24* (35), 11124–11131. <https://doi.org/10.1021/acs.nanolett.4c03543>.
- (35) Sun, S.; Lu, M.; Gao, X.; Shi, Z.; Bai, X.; Yu, W. W.; Zhang, Y. 0D Perovskites: Unique Properties, Synthesis, and Their Applications. *Advanced Science* **2021**, *8* (24). <https://doi.org/10.1002/advs.202102689>.
- (36) Faizan, M.; Bhamu, K. C.; Murtaza, G.; He, X.; Kulhari, N.; AL-Anazy, M. M.; Khan, S. H. Electronic and Optical Properties of Vacancy Ordered Double Perovskites  $A_2BX_6$  ( $A = \text{Rb, Cs}$ ;  $B = \text{Sn, Pd, Pt}$ ; and  $X = \text{Cl, Br, I}$ ): A First Principles Study. *Sci Rep* **2021**, *11* (1), 6965. <https://doi.org/10.1038/s41598-021-86145-x>.
- (37) Liu, Y.; Zhou, J.; Guan, Y.; Xiao, Y.; Dong, H.; Wu, F.; Huang, L. Atomic Insights into the Optoelectronic Properties of Vacancy-Ordered Double Perovskite Halide Semiconductors. *Appl Phys Lett* **2024**, *124* (4). <https://doi.org/10.1063/5.0179731>.
- (38) Ghorui, S.; Kangsabanik, J.; Aslam, M.; Alam, A. Optoelectronic and Transport Properties of Vacancy-Ordered Double-Perovskite Halides: A First-Principles Study. *Phys Rev Appl* **2024**, *21* (2), 024036. <https://doi.org/10.1103/PhysRevApplied.21.024036>.

- (39) Zhou, C.; Lin, H.; Tian, Y.; Yuan, Z.; Clark, R.; Chen, B.; van de Burgt, L. J.; Wang, J. C.; Zhou, Y.; Hanson, K.; Meisner, Q. J.; Neu, J.; Besara, T.; Siegrist, T.; Lambers, E.; Djurovich, P.; Ma, B. Luminescent Zero-Dimensional Organic Metal Halide Hybrids with near-Unity Quantum Efficiency. *Chem Sci* **2018**, *9* (3), 586–593. <https://doi.org/10.1039/C7SC04539E>.
- (40) Xie, L.; Qiu, H.; Chen, Y.; Lu, Y.; Chen, Y.; Chen, L.; Hu, S. Construction of a Zero-Dimensional Halide Perovskite in Micron Scale towards a Deeper Understanding of Phase Transformation Mechanism and Fluorescence Applications. *RSC Adv* **2024**, *14* (48), 35490–35497. <https://doi.org/10.1039/D4RA06404F>.
- (41) Li, M.; Xia, Z. Recent Progress of Zero-Dimensional Luminescent Metal Halides. *Chem Soc Rev* **2021**, *50* (4), 2626–2662. <https://doi.org/10.1039/D0CS00779J>.
- (42) Spek, A. L. Single-Crystal Structure Validation with the Program *PLATON*. *J Appl Crystallogr* **2003**, *36* (1), 7–13. <https://doi.org/10.1107/S0021889802022112>.
- (43) Krause, L.; Herbst-Irmer, R.; Sheldrick, G. M.; Stalke, D. Comparison of Silver and Molybdenum Microfocus X-Ray Sources for Single-Crystal Structure Determination. *J Appl Crystallogr* **2015**, *48* (1), 3–10. <https://doi.org/10.1107/S1600576714022985>.
- (44) Sheldrick, G. M. *SHELXT* – Integrated Space-Group and Crystal-Structure Determination. *Acta Crystallogr A Found Adv* **2015**, *71* (1), 3–8. <https://doi.org/10.1107/S2053273314026370>.
- (45) Sheldrick, G. M. Crystal Structure Refinement with *SHELXL*. *Acta Crystallogr C Struct Chem* **2015**, *71* (1), 3–8. <https://doi.org/10.1107/S2053229614024218>.
- (46) Dolomanov, O. V.; Bourhis, L. J.; Gildea, R. J.; Howard, J. A. K.; Puschmann, H. *OLEX2*: A Complete Structure Solution, Refinement and Analysis Program. *J Appl Crystallogr* **2009**, *42* (2), 339–341. <https://doi.org/10.1107/S0021889808042726>.
- (47) Momma, K.; Izumi, F. *VESTA 3* for Three-Dimensional Visualization of Crystal, Volumetric and Morphology Data. *J Appl Crystallogr* **2011**, *44* (6), 1272–1276. <https://doi.org/10.1107/S0021889811038970>.
- (48) Ketelaar, J. A. A.; Rietdijk, A. A.; van Staveren, C. H. Die Kristallstruktur von Ammonium-, Kalium-, Rubidium- Und Cäsiumstannibromid. *Recueil des Travaux Chimiques des Pays-Bas* **1937**, *56* (9), 907–908. <https://doi.org/10.1002/recl.19370560913>.

- (49) Murphy, A. B. Modified Kubelka–Munk Model for Calculation of the Reflectance of Coatings with Optically-Rough Surfaces. *J Phys D Appl Phys* **2006**, *39* (16), 3571–3581. <https://doi.org/10.1088/0022-3727/39/16/008>.
- (50) Wojdyr, M. *Fityk*: A General-Purpose Peak Fitting Program. *J Appl Crystallogr* **2010**, *43* (5), 1126–1128. <https://doi.org/10.1107/S0021889810030499>.
- (51) Clark, S. J.; Segall, M. D.; Pickard, C. J.; Hasnip, P. J.; Probert, M. I. J.; Refson, K.; Payne, M. C. First Principles Methods Using CASTEP. *Z Kristallogr Cryst Mater* **2005**, *220* (5–6), 567–570. <https://doi.org/10.1524/zkri.220.5.567.65075>.
- (52) Kohn, W.; Sham, L. J. Self-Consistent Equations Including Exchange and Correlation Effects. *Physical Review* **1965**, *140* (4A), A1133–A1138. <https://doi.org/10.1103/PhysRev.140.A1133>.
- (53) Hohenberg, P.; Kohn, W. Inhomogeneous Electron Gas. *Physical Review* **1964**, *136* (3B), B864–B871. <https://doi.org/10.1103/PhysRev.136.B864>.
- (54) Hamann, D. R.; Schlüter, M.; Chiang, C. Norm-Conserving Pseudopotentials. *Phys Rev Lett* **1979**, *43* (20), 1494–1497. <https://doi.org/10.1103/PhysRevLett.43.1494>.
- (55) Usman Ghani, M.; Sagir, M.; Bilal Tahir, M.; Elsaedy, H. I.; Nazir, S.; Alrobei, H.; Alzaid, M. CASTEP Investigation of Structural, Electronic, and Optical Properties of Halide Perovskites RbXCl<sub>3</sub> (X = Ge, Sn, Pb) for Solar Cell Applications. *Inorg Chem Commun* **2023**, *155*, 111007. <https://doi.org/10.1016/j.inoche.2023.111007>.
- (56) Sarker, Md. A.; Hasan, M. M.; Momin, Md. Al; Irfan, A.; Islam, Md. R.; Sharif, A. Band Gap Engineering in Lead Free Halide Cubic Perovskites GaGeX<sub>3</sub> (X = Cl, Br, and I) Based on First-Principles Calculations. *RSC Adv* **2024**, *14* (14), 9805–9818. <https://doi.org/10.1039/D4RA00224E>.
- (57) Hasan, N.; Arifuzzaman, M.; Kabir, A. Structural, Elastic and Optoelectronic Properties of Inorganic Cubic FrBX<sub>3</sub> (B = Ge, Sn; X = Cl, Br, I) Perovskite: The Density Functional Theory Approach. *RSC Adv* **2022**, *12* (13), 7961–7972. <https://doi.org/10.1039/D2RA00546H>.
- (58) Pfrommer, B. G.; Côté, M.; Louie, S. G.; Cohen, M. L. Relaxation of Crystals with the Quasi-Newton Method. *J Comput Phys* **1997**, *131* (1), 233–240. <https://doi.org/10.1006/jcph.1996.5612>.
- (59) Heyd, J.; Peralta, J. E.; Scuseria, G. E.; Martin, R. L. Energy Band Gaps and Lattice Parameters Evaluated with the Heyd-Scuseria-Ernzerhof Screened

- Hybrid Functional. *J Chem Phys* **2005**, *123* (17). <https://doi.org/10.1063/1.2085170>.
- (60) Heyd, J.; Scuseria, G. E. Efficient Hybrid Density Functional Calculations in Solids: Assessment of the Heyd–Scuseria–Ernzerhof Screened Coulomb Hybrid Functional. *J Chem Phys* **2004**, *121* (3), 1187–1192. <https://doi.org/10.1063/1.1760074>.
- (61) Heyd, J.; Scuseria, G. E. Assessment and Validation of a Screened Coulomb Hybrid Density Functional. *J Chem Phys* **2004**, *120* (16), 7274–7280. <https://doi.org/10.1063/1.1668634>.
- (62) Heyd, J.; Scuseria, G. E.; Ernzerhof, M. Hybrid Functionals Based on a Screened Coulomb Potential. *J Chem Phys* **2003**, *118* (18), 8207–8215. <https://doi.org/10.1063/1.1564060>.
- (63) Henderson, T. M.; Paier, J.; Scuseria, G. E. Accurate Treatment of Solids with the HSE Screened Hybrid. *physica status solidi (b)* **2011**, *248* (4), 767–774. <https://doi.org/10.1002/pssb.201046303>.
- (64) Izmaylov, A. F.; Scuseria, G. E.; Frisch, M. J. Efficient Evaluation of Short-Range Hartree-Fock Exchange in Large Molecules and Periodic Systems. *J Chem Phys* **2006**, *125* (10). <https://doi.org/10.1063/1.2347713>.
- (65) Kavanagh, S. R.; Savory, C. N.; Liga, S. M.; Konstantatos, G.; Walsh, A.; Scanlon, D. O. Frenkel Excitons in Vacancy-Ordered Titanium Halide Perovskites ( $\text{Cs}_2\text{TiX}_6$ ). *J Phys Chem Lett* **2022**, *13* (47), 10965–10975. <https://doi.org/10.1021/acs.jpcclett.2c02436>.
- (66) Ravidas, B. K.; Roy, M. K.; Samajdar, D. P. Design Insights and Photovoltaic Performance Analysis of Non-Lead Inorganic  $\text{RbSnX}_3$  ( $\text{X} = \text{I}, \text{Br}, \text{Cl}$ ) Perovskites through Coupled Density Functional Theory and *SCAPS-1D* Simulation Frameworks. *ACS Appl Electron Mater* **2024**, *6* (7), 5126–5150. <https://doi.org/10.1021/acsaelm.4c00670>.
- (67) Fu, J.; Ramesh, S.; Melvin Lim, J. W.; Sum, T. C. Carriers, Quasi-Particles, and Collective Excitations in Halide Perovskites. *Chem Rev* **2023**, *123* (13), 8154–8231. <https://doi.org/10.1021/acs.chemrev.2c00843>.
- (68) Ma, H.; Ma, Y.; Wang, H.; Slebodnick, C.; Alatas, A.; Urban, J. J.; Tian, Z. Experimental Phonon Dispersion and Lifetimes of Tetragonal  $\text{CH}_3\text{NH}_3\text{PbI}_3$  Perovskite Crystals. *J Phys Chem Lett* **2019**, *10* (1), 1–6. <https://doi.org/10.1021/acs.jpcclett.8b03419>.
- (69) Zhang, K.-C.; Shen, C.; Zhang, H.-B.; Li, Y.-F.; Liu, Y. Effect of Quartic Anharmonicity on the Carrier Transport of Cubic Halide Perovskites  $\text{CsSnI}_3$

and CsPbI<sub>3</sub>. *Phys Rev B* **2022**, *106* (23), 235202. <https://doi.org/10.1103/PhysRevB.106.235202>.

- (70) Torres, D. I.; Freire, J. D.; Katiyar, R. S. Lattice Dynamics of Crystals Having R<sub>2</sub>MX<sub>6</sub> Structure. *Phys Rev B* **1997**, *56* (13), 7763–7766. <https://doi.org/10.1103/PhysRevB.56.7763>.
- (71) Kaltzoglou, A.; Antoniadou, M.; Kontos, A. G.; Stoumpos, C. C.; Perganti, D.; Siranidi, E.; Raptis, V.; Trohidou, K.; Psycharis, V.; Kanatzidis, M. G.; Falaras, P. Optical-Vibrational Properties of the Cs<sub>2</sub>SnX<sub>6</sub> (X = Cl, Br, I) Defect Perovskites and Hole-Transport Efficiency in Dye-Sensitized Solar Cells. *The Journal of Physical Chemistry C* **2016**, *120* (22), 11777–11785. <https://doi.org/10.1021/acs.jpcc.6b02175>.
- (72) Kavanagh, S. R.; Savory, C. N.; Liga, S. M.; Konstantatos, G.; Walsh, A.; Scanlon, D. O. Frenkel Excitons in Vacancy-Ordered Titanium Halide Perovskites (Cs<sub>2</sub>TiX<sub>6</sub>). *J Phys Chem Lett* **2022**, *13* (47), 10965–10975. <https://doi.org/10.1021/acs.jpclett.2c02436>.
- (73) Ganesan, R.; Vinodhini, S. P.; Arulmozhi, R.; Muralidharan, R. Influence of Halogen Substitution in Double Perovskite Rb<sub>2</sub>Sn(Br<sub>0.75</sub>I<sub>0.25</sub>)<sub>6</sub> on the Photocatalytic Degradation of Methylene Blue Dye under Visible Light Irradiation. *Journal of Materials Science: Materials in Electronics* **2023**, *34* (2), 151. <https://doi.org/10.1007/s10854-022-09533-7>.
- (74) Schryver, S.; Lamichhane, A. Temperature-Driven Structural Phase Transitions in CsPbBr<sub>3</sub>. *Solid State Commun* **2023**, *371*, 115237. <https://doi.org/10.1016/j.ssc.2023.115237>.
- (75) Hoffman, A. E. J.; Saha, R. A.; Borgmans, S.; Puech, P.; Braeckvelt, T.; Roeffaers, M. B. J.; Steele, J. A.; Hofkens, J.; Van Speybroeck, V. Understanding the Phase Transition Mechanism in the Lead Halide Perovskite CsPbBr<sub>3</sub> via Theoretical and Experimental GIWAXS and Raman Spectroscopy. *APL Mater* **2023**, *11* (4). <https://doi.org/10.1063/5.0144344>.
- (76) Pelant, I.; Valenta, J. *Luminescence Spectroscopy of Semiconductors*; Oxford University PressOxford, 2012. <https://doi.org/10.1093/acprof:oso/9780199588336.001.0001>.
- (77) Hoye, R. L. Z.; Hidalgo, J.; Jagt, R. A.; Correa-Baena, J.; Fix, T.; MacManus-Driscoll, J. L. The Role of Dimensionality on the Optoelectronic Properties of Oxide and Halide Perovskites, and Their Halide Derivatives. *Adv Energy Mater* **2022**, *12* (4). <https://doi.org/10.1002/aenm.202100499>.
- (78) Makuła, P.; Pacia, M.; Macyk, W. How To Correctly Determine the Band Gap Energy of Modified Semiconductor Photocatalysts Based on UV–Vis

Spectra. *J Phys Chem Lett* **2018**, *9* (23), 6814–6817. <https://doi.org/10.1021/acs.jpcllett.8b02892>.

- (79) Soares, C. C. S.; Rodríguez-Hernández, J. S.; Gómez, Mayra. A. P.; Andrade, D. M.; Fechine, P. B. A.; Ayala, A. P.; Paschoal, C. W. A. Strong Electron–Phonon Coupling in Vacancy-Ordered Cs<sub>2</sub>SnBr<sub>6</sub> Double Perovskite. *J Mater Chem C Mater* **2024**. <https://doi.org/10.1039/D4TC01818D>.
- (80) Pal, D. A Comprehensive Analysis of Eco-Friendly Cs<sub>2</sub>SnI<sub>6</sub> Based Tin Halide Perovskite Solar Cell through Device Modeling. *Adv Theory Simul* **2023**, *6* (3). <https://doi.org/10.1002/adts.202200856>.
- (81) Tan, Z.; Pang, J.; Niu, G.; Yuan, J.-H.; Xue, K.-H.; Miao, X.; Tao, W.; Zhu, H.; Li, Z.; Zhao, H.; Du, X.; Tang, J. Tailoring the Electron and Hole Dimensionality to Achieve Efficient and Stable Metal Halide Perovskite Scintillators. *Nanophotonics* **2021**, *10* (8), 2249–2256. <https://doi.org/10.1515/nanoph-2020-0624>.
- (82) Kahmann, S.; Tekelenburg, E. K.; Duim, H.; Kamminga, M. E.; Loi, M. A. Extrinsic Nature of the Broad Photoluminescence in Lead Iodide-Based Ruddlesden–Popper Perovskites. *Nat Commun* **2020**, *11* (1), 2344. <https://doi.org/10.1038/s41467-020-15970-x>.
- (83) Duan, D.; Ge, C.; Rahaman, M. Z.; Lin, C.-H.; Shi, Y.; Lin, H.; Hu, H.; Wu, T. Recent Progress with One-Dimensional Metal Halide Perovskites: From Rational Synthesis to Optoelectronic Applications. *NPG Asia Mater* **2023**, *15* (1), 8. <https://doi.org/10.1038/s41427-023-00465-0>.
- (84) Stoneham, A. M. *Theory of Defects in Solids: Electronic Structure of Defects in Insulators and Semiconductors*; Oxford University Press, 2001.
- (85) Toyozawa, Y. *Optical Processes in Solids*; Cambridge University Press, 2003. <https://doi.org/10.1017/CBO9780511615085>.
- (86) Stoneham, A. M.; Gavartin, J.; Shluger, A. L.; Kimmel, A. V; Ramo, D. M.; Rønnow, H. M.; Aepli, G.; Renner, C. Trapping, Self-Trapping and the Polaron Family. *Journal of Physics: Condensed Matter* **2007**, *19* (25), 255208. <https://doi.org/10.1088/0953-8984/19/25/255208>.
- (87) Schmidt, T.; Lischka, K.; Zulehner, W. Excitation-Power Dependence of the near-Band-Edge Photoluminescence of Semiconductors. *Phys Rev B* **1992**, *45* (16), 8989–8994. <https://doi.org/10.1103/PhysRevB.45.8989>.
- (88) Leroux, M.; Grandjean, N.; Beaumont, B.; Nataf, G.; Semond, F.; Massies, J.; Gibart, P. Temperature Quenching of Photoluminescence Intensities in

Undoped and Doped GaN. *J Appl Phys* **1999**, 86 (7), 3721–3728. <https://doi.org/10.1063/1.371242>.

- (89) Hansen, K. R.; McClure, C. E.; Powell, D.; Hsieh, H.; Flannery, L.; Garden, K.; Miller, E. J.; King, D. J.; Sainio, S.; Nordlund, D.; Colton, J. S.; Whittaker-Brooks, L. Low Exciton Binding Energies and Localized Exciton–Polaron States in 2D Tin Halide Perovskites. *Adv Opt Mater* **2022**, 10 (9). <https://doi.org/10.1002/adom.202102698>.
- (90) Li, Y.; Zhou, H.; Xia, M.; Shen, H.; Wang, T.; Gao, H.; Sheng, X.; Han, Y.; Chen, Z.; Dou, L.; Zhu, H.; Shi, E. Phase-Pure 2D Tin Halide Perovskite Thin Flakes for Stable Lasing. *Sci Adv* **2023**, 9 (32). <https://doi.org/10.1126/sciadv.adh0517>.
- (91) Rudin, S.; Reinecke, T. L.; Segall, B. Temperature-Dependent Exciton Linewidths in Semiconductors. *Phys Rev B* **1990**, 42 (17), 11218–11231. <https://doi.org/10.1103/PhysRevB.42.11218>.
- (92) Yu, P. Y.; Cardona, M. *Fundamentals of Semiconductors*; Springer Berlin Heidelberg: Berlin, Heidelberg, 2010. <https://doi.org/10.1007/978-3-642-00710-1>.
- (93) Zhang, T.; Zhou, C.; Feng, X.; Dong, N.; Chen, H.; Chen, X.; Zhang, L.; Lin, J.; Wang, J. Regulation of the Luminescence Mechanism of Two-Dimensional Tin Halide Perovskites. *Nat Commun* **2022**, 13 (1), 60. <https://doi.org/10.1038/s41467-021-27663-0>.
- (94) Iaru, C. M.; Brodu, A.; van Hoof, N. J. J.; ter Huurne, S. E. T.; Buhot, J.; Montanarella, F.; Buhbut, S.; Christianen, P. C. M.; Vanmaekelbergh, D.; de Mello Donega, C.; Rivas, J. G.; Koenraad, P. M.; Silov, A. Yu. Fröhlich Interaction Dominated by a Single Phonon Mode in CsPbBr<sub>3</sub>. *Nat Commun* **2021**, 12 (1), 5844. <https://doi.org/10.1038/s41467-021-26192-0>.
- (95) Zhou, X.; Zhang, Z. Electron–Phonon Coupling in CsPbBr<sub>3</sub>. *AIP Adv* **2020**, 10 (12). <https://doi.org/10.1063/5.0017149>.
- (96) Toyozawa, Y. Theory of Line-Shapes of the Exciton Absorption Bands. *Progress of Theoretical Physics* **1958**, 20 (1), 53–81. <https://doi.org/10.1143/PTP.20.53>.
- (97) Toyozawa, Y. Further Contribution to the Theory of the Line-Shape of the Exciton Absorption Band. *Progress of Theoretical Physics* **1962**, 27 (1), 89–104. <https://doi.org/10.1143/PTP.27.89>.
- (98) Chen, B.; Chen, R.; Huang, B. Strong Electron–Phonon Coupling Induced Self-Trapped Excitons in Double Halide Perovskites. *Advanced Energy and*

*Sustainability Research* **2023**, *4* (9).  
<https://doi.org/10.1002/aesr.202300018>.

- (99) Chen, B.; Chen, R.; Huang, B. Strong Electron–Phonon Coupling Induced Self-Trapped Excitons in Double Halide Perovskites. *Advanced Energy and Sustainability Research* **2023**, *4* (9).  
<https://doi.org/10.1002/aesr.202300018>.
- (100) Lanzani, G. *The Photophysics behind Photovoltaics and Photonics*, First Edition.; Wiley, 2012. <https://doi.org/10.1002/9783527645138>.
- (101) Vogelsang, H.; Husberg, O.; Köhler, U.; von der Osten, W.; Marchetti, A. P. Exciton Self-Trapping in AgCl Nanocrystals. *Phys Rev B* **2000**, *61* (3), 1847–1852. <https://doi.org/10.1103/PhysRevB.61.1847>.
- (102) Manser, J. S.; Christians, J. A.; Kamat, P. V. Intriguing Optoelectronic Properties of Metal Halide Perovskites. *Chem Rev* **2016**, *116* (21), 12956–13008. <https://doi.org/10.1021/acs.chemrev.6b00136>.
- (103) Hazra, V.; Mandal, A.; Bhattacharyya, S. Optoelectronic Insights of Lead-Free Layered Halide Perovskites. *Chem Sci* **2024**, *15* (20), 7374–7393. <https://doi.org/10.1039/D4SC01429D>.
- (104) Maughan, A. E.; Ganose, A. M.; Scanlon, D. O.; Neilson, J. R. Perspectives and Design Principles of Vacancy-Ordered Double Perovskite Halide Semiconductors. *Chemistry of Materials* **2019**, *31* (4), 1184–1195. <https://doi.org/10.1021/acs.chemmater.8b05036>.